ISSN (ONLINE): 2454-9762
ISSN (PRINT): 2454-9762
Available online at www.ijarmate.com

International Journal of Advanced Research in Management, Architecture, Technology and Engineering (IJARMATE)
Vol. 3, Special Issue 10, March 2017

ANALYSIS AND DESIGN OF GRID CONNECTED PHOTOVOLTAIC SYSTEM USING ONLINE VARIABLE TOPOLOGY

Benisha.B[1], C. Gnana Thilaka[2]
[1]PG student, Power Electronics and Drives, Ponjesly College of Engineering
[2]Assistant Professor, Department of EEE, Ponjesly College of Engineering

***Abstract*—photovoltaic gridconnected generation system, the key focus is how to expand the generation range of the PV array and enhance the total efficiency of the system. This project originally derived expressions of the total loss and grid current total harmonics distortions of cascaded inverter and H-bridge inverter under the conditions of variable output voltage and power of PV array. It is proved that, compared with H-bridge inverter, the operation range of the cascaded inverter is wider, while the total loss is larger. Furthermore, a novel online variable topology-type grid-connected inverter is proposed. A bidirectional power switch is introduced into the conventional cascaded inverter to connect the negative terminals of the PV arrays. When the output voltages of PV arrays are lower, the proposed inverter works under cascaded inverter mode to obtain wider generation range. When the output voltages of PV arrays are higher, the proposed inverter is transformed into equivalent H-bridge inverter mode to reduce the total loss. Thus, wider generation range and higher efficiency are both implemented.**

***Index Terms*—Grid-connected inverter, photovoltaicgeneration, online variable topology, efficiency**

I. INTRODUCTION

The advantages of clean electricity production, harmlessness for the environment and reduction of the dependence on polluting fossil fuels, photovoltaic grid connected generation system have attracted great attention and grown rapidly [12],[16]. Current research focuses on enhancing the energy production and increasing its total efficiency to reduce the initial investment cost and occupied space.

In practice application, however, the output voltage and power of PV array change in a wide range with the variation of atmospheric temperature and solar irradiance. In order to widen the generation range of PV-GGS, power electronic conversion is commonly used. In existing literature, a variety of PV-GGS structures are introduced based on various kinds of power electronics devices, including single-stage two-level grid connected inverter [8], two-stage grid-connected inverter [5], single-stage multi-level grid-connected inverter [4,11] and Z-source grid-connected inverter [9]. The structure of single stage inverter is simple while the generation range is smaller and the system utilization is decreased. In two-stage inverter, the DC voltage control link is added into the system to widen the generation range. In single-stage multi-level inverter system, a plurality of PV array work equivalently in series, thereby increasing the DC voltage and the operation range of the system is expanded. Although the aforementioned structures widen the generation range of PV-GGS, the inverter loss increases due to the larger number of devices and complex structure. Z-source inverter uses the shoot through state of the leg of DC-AC inverter to realize the boost control of DC voltage without DC-DC converters. However, the added cross impedance network also produces additional loss. Meanwhile the maximum system power level is limited due to the power rating and volume of added devices.

All the PV-GGSs above are based on traditional power electronics technique and there exists the following problems: Due to the wide input range of PV-GGS, in order to guarantee the safety and stability, the power level of the power components and filter inductor are selected from the maximum output power. While the filter inductor is designed from the requirement, that the grid current total harmonics distortion should meet the special standards even under the minimum grid current amplitude conditions. A bigger filter inductor value is required. It results in lower system utilization, higher volume and cost. Over a wide operation range, the inverter topology remains unchanged, all of the power switches involved in the system are always under working state, resulting in a large amount of loss, and the European efficiency decreasing obviously.

The expressions of the total losses and grid current THDs of cascaded multilevel grid-connected inverter and H-bridge grid-connected inverter corresponding to the output DC voltage and power of the PV array are derived for the first time under the condition that the output voltage and generation power of PV array are variable. It is proved that, the operation range of CM-GCI is wider, while the total loss is larger than HB-GCI. Furthermore, a novel online variable topology-type grid-connected inverter is proposed based on CM-GCI. When the output voltage of PV array is lower, OVT-GCI works under CMGCI mode to expand the lowest generation range of the PV array. When the output voltage of PV array is higher, the system transforms to HB-GCI mode to decrease the inverter loss. The proposed inverter topology achieves the system operating under a wider generation range and only employs single-stage inverter topology to implement higher efficiency.

II. ONLINE VARIABLE TOPOLOGY

In order to compare the total operation efficiencies of different PV-GGSes with a single value rather than using efficiency curves, the weighted efficiency concept of

ISSN (ONLINE): 2454-9762
ISSN (PRINT): 2454-9762
Available online at www.ijarmate.com

International Journal of Advanced Research in Management, Architecture, Technology and Engineering (IJARMATE)
Vol. 3, Special Issue 10, March 2017

"European efficiency" with weighted factors of various output power levels directly related to local radiation levels.

$$\eta_{EURO} = 0.03\eta_{5\%} + 0.06\eta_{10\%}0.13\eta_{20\%} + 0.1\eta_{30\%} + 0.48\eta_{50\%} + 0.2\eta_{100\%} \quad (1)$$

Where, $\eta_{x\%}$ is the conversion efficiency at the x percent ofinverter rated power. η_{EURO} is the total efficiency ofPV-GGS within the whole operation range.

In order to enhanceη_{EURO}, the total operation range of thePV-GGS should be expanded and the operation efficiencieswith various output power should be increased as well. Fromthe above analysis, if the PV-GGS operates under CM-GCImode when the output voltage and power of PV array arelower and under HB-GCI mode when system meets thevoltage constraint and current THD requirements, it should beobtained to widen the PV-GGS operation range as well asincrease the system efficiency, namely the Europeanefficiency.

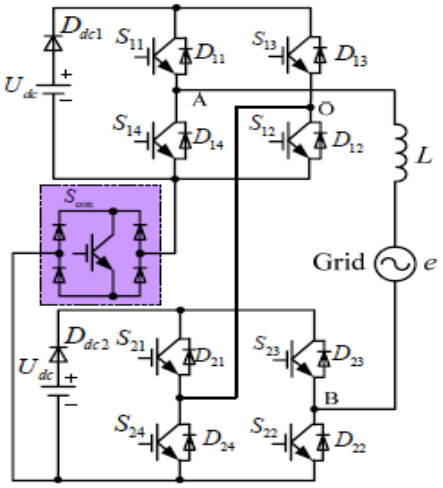

Fig. 1 Schematic of OVT-GCI

The main contribution is proposing an online variable topology to obtain the goals in Fig.1 the proposed OVT-GCI is based on the five-level CM-GC. Two H-bridge inverters are connected in series with a bidirectional power switch con *S* connecting the negative terminals of the two inverters. When con *S* is off, the topology is a traditional five-level CM-GCI. When con *S* is on, meanwhileS_{14}, $S_{11}$are on andS_{12},$S_{24}$are off, the positive and negative terminals of the two DC sources are connected respectively, and the topology is transformed into equivalent HB-GCI mode.

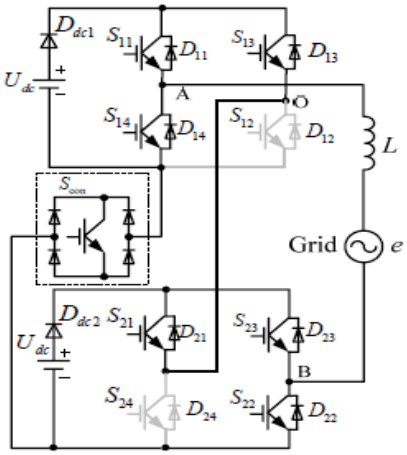

Fig. 2 Schematic of HB-GCI mode

The reason of calling the inverter Fig. 2 is "equivalent HB-GCI mode" is that, compared to the standard HB-GCI, some additional power switches are introduced. In the following, the working process of the equivalent HB-GCI is analyzed and then the additional conduction loss is calculated to evaluate the practicability and advantage of the proposed OVT-GCI. In Fig. 3, Fig. 4 and Fig. 5 Within each carrier cycle, the state of the output voltage of the equivalent HB-GCI changes 4 times, denoted as State 1-4, respectively. During State 1 and 3, the energy is transmitted from DC sources to the grid while during State 2 and 4, the inverter is under freewheeling state.

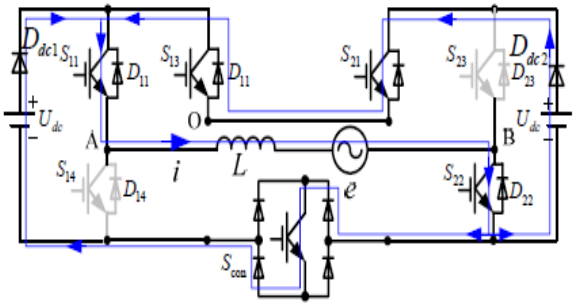

Fig. 3 Equivalent circuits of equivalent HB-GCI mode of State 1 and 3

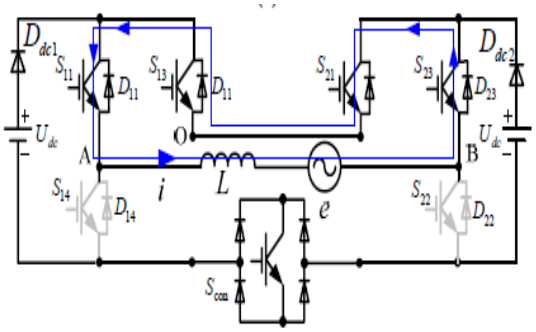

ISSN (ONLINE): 2454-9762
ISSN (PRINT): 2454-9762
Available online at www.ijarmate.com

International Journal of Advanced Research in Management, Architecture, Technology and Engineering (IJARMATE)
Vol. 3, Special Issue 10, March 2017

Fig. 4 Equivalent circuits of equivalent HB-GCI mode of State 2

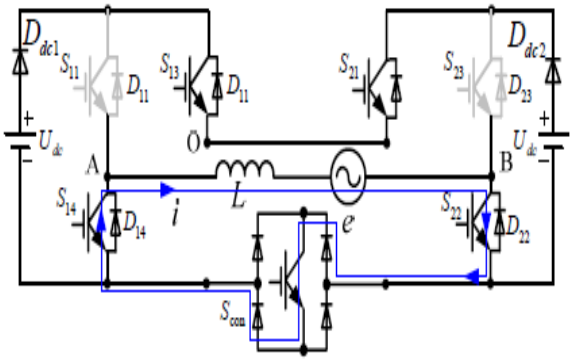

Fig. 5 Equivalent circuits of equivalent HB-GCI mode of State 4

The current flowing routes are different and the number of conduction-state power components and the currents flowing through them are not identical that shown in Table.1. The conduction loss of additional power components within one carrier cycle is calculated.

$$P_{con\_add} = \left(1 - \frac{D_{HBI}}{2}\right) U_{ceoI} i + \left(1 - \frac{3D_{HBI}}{4}\right) R_{onI} i^2 + \left(\frac{1}{2} - \frac{3D_{HBI}}{4}\right) U_{FOD}\, i + \left(\frac{1}{2} - D_{HBI}\right) R_{onD} i^2 \quad (2)$$

The average conduction loss of additional power components

Table 1 Various States of HB-GCI

State	IGBT	Diode	Current	Duty cycle
1 and 3	2	3	$0.5i$	D_{HBI}
2	1	1	i	$1 - D_{HBI}$
4	1	2	i	$1 - D_{HBI}$

Table 3.1 Shows the Flowing Current, Duty Cycle and Number of Additional Conduction Power Components of Various States of H-bridge inverter

Within one fundamental cycle is calculated as

$$\bar{P}_{con\_add} = \frac{2}{\pi}\int_0^{\frac{\pi}{2}} P_{con\_add}\, d(\omega t)$$

$$= \left(\frac{1}{\pi} - \frac{M}{8}\right) U_{ceoI} I_m + \left(\frac{1}{8} - \frac{3M}{8\pi}\right) R_{onI} I_m^2 + \left(\frac{3}{\pi} - \frac{3M}{4}\right) U_{FOD} I_m + \left(\frac{3}{4} - \frac{8M}{3\pi}\right) R_{onD} I_m^2 \quad (3)$$

The difference of the total conduction losses of CM-GCI and equivalent HB-GCI after considering the additional conduction loss is calculated as

$$\Delta\bar{p}_{con} = \bar{P}_{con\_IGBT1} + \bar{P}_{con\_diode1} - \left(\bar{P}_{con\_IGBT2} + \bar{P}_{con\_diode2} + \bar{P}_{con\_add}\right)$$

$$= \frac{M}{2} U_{ceoI} I_m + \frac{3M}{8} R_{onI} I_m^2 + \left(\frac{3M}{4} - \frac{1}{\pi}\right) U_{FOD} I_m + \left(\frac{8M}{3\pi} - \frac{1}{4}\right) R_{onD} I_m^2 \quad (4)$$

The polarity of *con* $\Delta\bar{p}_{con}$ is analyzed as follows. According to the datasheet of power component, $U_{FOD} \approx {}^{U_{ceoI}}/_{2}$ and $R_{onI} \approx R_{onD}$, then when M meets the following condition,

$$\Delta\bar{p}_{con} > 0.M > \left(\frac{1}{3\pi} + \frac{1}{4}\frac{R_{onI} I_m}{U_{ceoI}}\right) / \left(\frac{14}{3\pi} + \frac{7}{8}\right) \quad (5)$$

Similarly, known as from the datasheet, under rated current conditions, $R_{onI} I_{m_{rate}} / U_{ceoI} < 0.1$, substituting this value into eqn.(5), M >0.078 is solved. It means that when M changes within a wide range, the conduction loss of equivalent HBGCI is always smaller than the one of CM-GCI. As a result, through transforming the topology from CM-GCI into HBGCI, the European efficiency of the system still is enhanced.

The diodes D_{dc1} and D_{dc2} connected in series between the DC sources and the inverters have been existed in the PV arrays but not added by the proposed topology. In the actual PV-GGS, many PV panels are usually connected in parallel to increase total output power. In order to avoid the circular circuit among various parallel strings, a diode with lower loss is connected in-series in the output of every parallel string. The diode is namely the D_{dc1} or D_{dc2}. In the equivalent HB-GCI mode, the two DC sources are connected in parallel. Because of the existence of D_{dc1} and D_{dc2}, the circular circuit between the two DC sources in OVT-GCI is avoided. To illustrate it more clearly, D_{dc1} and D_{dc2} are drawn. On the hand, because the two DC sources are connected in parallel in HB-GCI mode, it is required that the output characteristics of the DC sources are as same as possible to reduce the energy discount. In a method to guarantee the output characters of paralleled PV panels uniform in PVGGS is introduced. The PV panels are sorted during manufacturing process, taking the ones with similar characters compose the PV panels. It takes the PV panels own 3% tolerant ability in output power.

The principle of the OVT-GCI is further depicted in Fig. 6. When the output voltage of PV array is lower, OVTGCI works under CM-GCI mode to extend the generation range, while when the output voltage is higher, OVT-GCI works under equivalent HB-GCI mode to enhance the system efficiency. The aspects of the modulation strategy of the two modes and the online transformation between them should be considered. For the CM-GCI mode, the conventional CPSSPWM is adopted while for the equivalent HB-GCI mode, in order to increase the utility of the controller, the reusable modulation strategy is used. With this kind of modulation strategy, the carrier and modulation wave generation units and the compare unit for controlling the CMGCI are also used to generate control signals of HB-GCI. The difference is only that the mapping between the control signals and the actual physical I/O ports should be redefined.

ISSN (ONLINE): 2454-9762
ISSN (PRINT): 2454-9762
Available online at www.ijarmate.com

International Journal of Advanced Research in Management, Architecture, Technology and Engineering (IJARMATE)
Vol. 3, Special Issue 10, March 2017

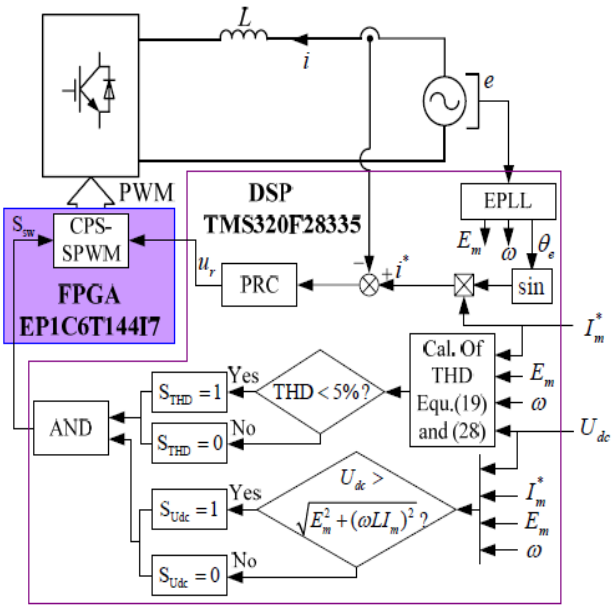

Fig. 6 Sketch of the implementation platform of the proposed OVT-GCI.

As a result, occupancy of the resource of controller is reduced and the complexity for implementing the modulation strategy is simplified as well. Additionally, in order to avoid the current overshoot during the process of transforming the two modes, it is performed at zero-crossing point of modulation wave. As the system is commonly controlled under unity power factor, the phase difference between inverter output voltage and grid current is very small, and the grid current value is low as well at the zero-crossing point, hence the topology transformation will not cause obvious current overshoot.

The modulation scheme and transforming control of the two topologies are performed in FPGA, and other control schemes are implemented in DSP. Single close loop control of grid current based on proportional-resonant controller (PRC) is implemented in this system. The amplitude, frequency and phase angle θ_e of grid voltage are estimated by the enhanced phase locked loop (EPLL). The requirement of system operating in HB-GCI mode is to meet 2 $U_{dc} > \sqrt{E_m^2 + (\omega L I_m)^2}$ and current THD <5%. Therefore, the judgments on the two requirements are made respectively according to actual DC voltage and grid current. The modulation signal u_r output by the PR controller and solved transforming signal S_{sw} then input the reusable CPS-SPWM to obtain the control signals of various power components.

An adjustable autotransformer connected in series with an isolated transformer with dual outputs is deployed and connected with diode-based rectifier and capacitor filter circuit to obtain two identical adjustable DC sources to supply power for the inverter. The total loss of inverter is tested by power analyzer WT1800.

The performance of OVT-GCI under a wide DC output voltage range is performed. The DC voltage at transforming point of the two modes is approximately 380V

51 :ding to the foregoing calculation, when the current THD 3-GCI mode satisfies the grid-connected standards. The inverter operates in CM-GCI mode when DC voltage is lower. The output of inverter is five-level and the grid current increases gradually with the DC voltage rising. The efficiency gets a bit lower, but increases significantly when the system transforms to HB-GCI. Throughout the entire operation process, the grid current remains sinusoidal and is out phase with the grid voltage. During the transforming process, there is almost no current overshoot as the transformation of the topology is performed at zero-crossing point. In CM-GCI mode, the spectral distribution of grid current is concentrated at four times the carrier frequency and its integer multiples zones, while in HBGCI mode, the spectral distribution of grid current is concentrated at double times the carrier frequency and its integer multiples zones, as is also consistent with the foregoing analysis.

Moreover, the grid current THD curve and efficiency distribution curve are consistent with the aforementioned theoretical analysis results, which illustrate the accuracy of the foregoing analysis. Throughout the entire operation process, the grid current THD is limited within 5%. European efficiency of inverter is further calculated. The European efficiency of CM-GCI is 93.2% and the European efficiency of the proposed topology is 95.8 % with an increase of 2.6 %.

III. LOSSES AND CURRENT THDS OF CM-GCI AND HB-GCI

To compare the losses and current THDs of the two inverters in a compact way, and to simplify the implementation of subsequent proposed new inverter topology, a reusable carrier phase shifted sinusoidal pulse width modulation (CPS-SPWM) scheme is proposed. For the CM-GCI, the conventional CPS SPWM is utilized. As for the HB-GCI, The control signals for s_{11} and s_{14} are obtained by comparing T_{r1} with r_u, while the control signals for s_{21} and s_{23} are obtained by comparing T_{r2} with r_u. By adopting the proposed modulation scheme, the whole cycle output voltage of HB-GCI will be three-level. The equivalent switching frequency of the output voltage is

$$f_{s2} = 1/T_{s2} = 2 \cdot f_c$$

Where, f_c is the carrier frequency

The schematics of CM-GCI and HB-GCI are shown in Fig.7 and 8

ISSN (ONLINE): 2454-9762
ISSN (PRINT): 2454-9762
Available online at www.ijarmate.com

International Journal of Advanced Research in Management, Architecture, Technology and Engineering (IJARMATE)
Vol. 3, Special Issue 10, March 2017

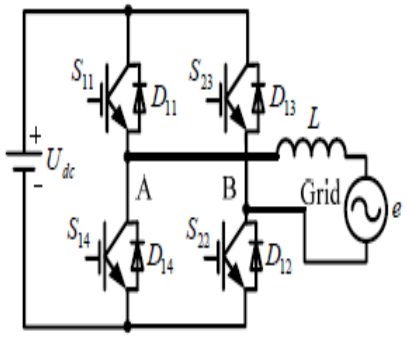

Fig. 7 Schematics of HB-GCI

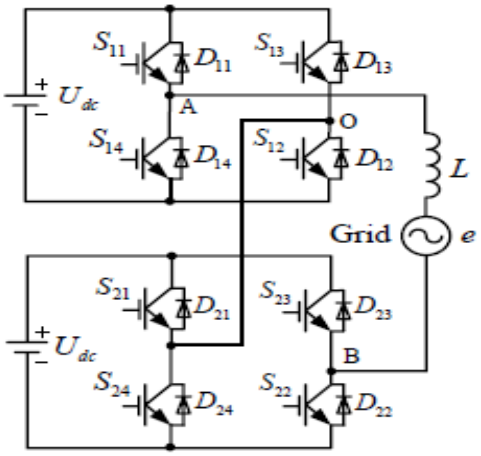

Fig. 8 Schematics of CM-GCI

Fig. 7 H-bridge Grid Connected Inverter consists of four switches and four diodes. Fig. 8 the cascaded multilevel inverter consists of a series of H-bridge inverter units.

Table 2 Number of Conduction-States of CM-GCI

U_{AB}	$2U_{dc}$	U_{dc}	0	$-U_{dc}$	$-2U_{dc}$
Number of IGBT	4	3	2	3	4
Number of diode	0	1	2	1	0

Table 2 shows the Fig. 3.9 cascaded inverter's Conduction-State Power Components of Various Output Voltages of CM-GCI

The losses and current THDs of the two inverters are analyzed in the following. As the waveforms of the output voltage and current are 1/4 cycle symmetrical, only the case of phase angle region of [0, π / 2] is considered

1.Calculation of Total Loss and Current THD of CM-GCI

a. Principle of CPS-SPWM for CM-GCI

The amplitude modulation ratio of CM-GCI is defined as

$$M = \sqrt{E_m^2 + (\omega L I_m)^2} / (2U_{dc}) \quad (6)$$

Where, E_m isthe amplitude of the grid voltage,ω is the frequency of the grid voltage, I_m is the amplitude of grid current, L is the filter inductor, U_{dc} is the voltage of DC supply source.

Considering that the grid-connected inverter is controlled under unit power factor, the phase difference between the inverter output voltage and the grid voltage is ignored to simplify the analysis of loss. Then the modulation wave is defined as

$$u_r = M \sin(\omega t) \quad (7)$$

According to the principle of CPS-SPWM, when M>0.5 and $\omega t \in (0, \theta)$ ($\theta = \arcsin(1/2M)$) or $M \leq 0.5$, the duty cycle of the output voltage can be expressed as

$$D_{CM1}(\omega t) = 2M \sin(\omega t) \quad (8)$$

When M>0.5 and $\omega t \in (0, \pi/2)$ the duty cycle is

$$D_{CM2}(\omega t) = 2M \sin(\omega t) - 1 \quad (9)$$

When the output voltage of inverter (u_{AB}) is different, the numbers of IGBTs and diodes under conduction state are different as well. By analyzing the equivalent current flowing routes of various output voltages, the numbers of the conduction-state IGBTs and freewheeling diodes corresponding to various output voltages are obtained.

b. Grid Current Ripple

The following part is a analysis of the current ripple, as it is the loss of the inductor and the current THD. Within each switching cycle, according to the voltage equation of the inverter, the peak value of current ripple (Δi_{CM1}or Δi_{CM2}) as

$$\begin{cases} \Delta i_{CM1} = \frac{1}{4Lf_c}[U_{dc} - E_m \sin(\omega t)]D_{CM1}M > 0.5, \omega t \in (0,\theta) \text{ or } M \leq 0.5 \\ \Delta i_{CM2} = \frac{1}{4Lf_c}[2U_{dc} - E_m \sin(\omega t)]D_{CM2}M > 0.5 \text{ and } \omega t \in (0, \pi/2) \end{cases} \quad (10)$$

c. Total Average Conduction Losses of IGBTs and Diodes

The instantaneous conduction losses of IGBTs and diodes can be expressed linearly as

$$P_{con\ IGBT} = U_{ceI} i = (U_{ceo1} + R_{onI} i) i \quad (11)$$

$$P_{con\ diode} = U_F i = (U_{FOD} + R_{onD} i) i \quad (12)$$

Where, U_{ceo1} is the conduction saturation voltage drop of IGBT, R_{onI} is the conduction-state resistor of IGBT, U_{FOD} is the conduction saturation voltage drop of diode, R_{onD}, is the conduction-state resistor of diode $i = I_m \sin(\omega t)$ is the grid current.

The total average conduction losses of IGBTs and diodes during one fundamental cycle are calculated from Table 3.2 as

$$\bar{P}_{con\_IGBT1} = \left(\frac{4}{\pi} + M\right) U_{ceo1} I_m + \left(1 + \frac{8M}{3\pi}\right) R_{onI} I_m^2 \quad (13)$$

$$\bar{P}_{con\_diode1} = \left(\frac{4}{\pi} - M\right) U_{FOD} I_m + \left(1 - \frac{8M}{3\pi}\right) R_{onD} I_m^2 \quad (14)$$

ISSN (ONLINE): 2454-9762
ISSN (PRINT): 2454-9762
Available online at www.ijarmate.com

International Journal of Advanced Research in Management, Architecture, Technology and Engineering (IJARMATE)
Vol. 3, Special Issue 10, March 2017

d. Total Average Switching Losses of IGBTs and Diodes

Within any switching cycle, there is one IGBT turned off, one IGBT turned on, one diode turned off and one diode turned on. Because the turn-on loss of the diode is very small, it is neglected. The turn-on and turn-off losses of the IGBT and the turn-off loss of the diode are calculated. Based on the datasheet of IGBT provided by the manufacturer, the curves of the relationship among the turn-on and turn-off loss energy of the IGBT, the turn-off loss energy of the diode, the flowing current and the turn-off voltage of the IGBT are obtained. Then E_{ts} is the sum of turn-on loss and turn-off loss energy of IGBT, and turn-off loss energy of diode. E_{ts} can be calculated from

$$E_{ts} = E_{tsL}\frac{i(\omega t)}{I_{cs}}\frac{U_{dc}}{U_{csp}} \quad (15)$$

Where, E_{tsL} is the turn-off voltage crossing the IGBT, I_{cs} is the current flowing through the IGBT, E_{tsL} can be read from the loss curves afforded by the datasheet with I_{cs} and U_{csp}. The switching loss can be calculated from dividing E_{ts} by one switching period then the total average switching loss during one fundamental cycle is calculated as

$$P_{sw\_s} = \frac{1}{\pi} f_s \int_0^{\pi} E_{ts}\, d(\omega t) = \frac{6}{\pi} f_s E_{tsL}\frac{I_m}{I_{cs}}\cdot\frac{U_{dc}}{U_{csp}} \quad (16)$$

e. Loss of Filter Inductor

The loss of filter inductor is composed of the copper loss, the fundamental frequency iron loss and the high frequency iron loss. Among them, the copper loss is approximately directly proportional to the square of the RMS value of the grid current, and it can be expressed as

$$P_{L\_cop} = R_L I_m^2/2 \quad (17)$$

Where, R_L is the copper resistor of filter inductorTheFeSiAl magnetic powder core is selected as the core of the filter inductor. The fundamental iron loss is calculated based on Steinmetz equation as

$$P_{L\_cf} = 0.026 f_g^{1.008} B_g^{2.133} VOL_L \quad (18)$$

Where, B_g is the magnetic flux density, $f_g = 2\pi/\omega$ is the grid frequency, VOL_L is the volume of filter inductor

The high frequency iron loss is directly related to the high frequency magnetic flux ripple peak ΔB_{fs}. To simplify the analysis, the specific loss of the core material and the average of ΔB_{fs} within one fundamental cycle are quadratic fit. First, ΔB_{fs} is calculated. During each switching cycle, the relationship between ΔB_{fs} and the grid current ripple Δi can be expressed as

$$\Delta B_{fs} = L\Delta i/(NA_e) \quad (19)$$

Where, N is the turns of inductor coil, A_e is the sectional area of the inductor core.

From eqn.(10), when M>0.5, the average of ΔB_{fs} can be calculated as

$$\overline{\Delta B_{fs1}} = \frac{L}{NA_e}\cdot\frac{2}{\pi}\left\{\int_0^{\theta}\Delta i_{cm1}d(\omega t) + \int_{\theta}^{\frac{\pi}{2}}\Delta i_{cm2}d(\omega t)\right\} \quad (20)$$

$$= \frac{1}{2\pi NA_e f_s}\left[2MU_{dc} - \pi ME_m + (2MU_{dc} + E_m)\cos\theta - U_{dc}(\pi - 2\theta)\right]$$

When $M \le 0.5$, the average of ΔB_{fs} can be calculated as

$$\overline{B_{fs2}} = \frac{M}{2\pi NA_e f_s}\left(2U_{dc} - \frac{\pi}{2}E_m\right) \quad (21)$$

The fitted curve of specific loss can be expressed as

$$P_{cv} = f_s\left(a\overline{\Delta B_{fs}^2} + b\overline{\Delta B_{fs}} + c\right) \quad (22)$$

Where a, b and c are the fitting parameters and determined by the actual specific loss curve of the core material. Then the high frequency iron loss of filter inductor is calculated as

$$P_{L\_h} = P_{cv}V_L \quad (23)$$

f. Grid Current THD

By definition, the relationship between current THD and current ripples can be expressed as

$$THD = \sqrt{I_1^2 + I_2^2 + I_3^2 + I_4^2 + \cdots}/I_1 \approx \Delta I_{rms}/I_1 \quad (24)$$

Where, I_1 is the RMS value of the fundamental component of the grid current, I_i (i=2,3,...) is the harmonic component of the grid current. ΔI_{rms} is the RMS value of the actual grid current ripple.

2. Calculation of Total Loss and Current THD of HB-GCI

The duty cycle of HB-GCI is obtained as

$$D_{HBI(\omega t)} = 2M\sin(\omega t) \quad (25)$$

Similarly, the grid current ripple within one switching cycle yields

$$\Delta i_{HBI} = \frac{1}{2Lf_s}\left[U_{dc} - E_m\sin(\omega t)\right]D_{HBI} \quad (26)$$

During the whole fundamental cycle, it is equivalent that, one IGBT holds conduction-state, another IGBT works with the duty cycle of D_{HBI}. One diode works with the duty cycle of $(1 - D_{HBI})$.Then the total average conduction losses of the IGBTs and diodes are calculated as

$$\bar{P}_{con\_IGBT2} = \left(\frac{2}{\pi} + M\right)U_{ceol}I_m + \left(\frac{1}{2} + \frac{8M}{3\pi}\right)R_{on1}I_m^2 \quad (27)$$

$$\bar{P}_{con\_diode1} = \left(\frac{2}{\pi} - M\right)U_{FOD}I_m + \left(\frac{1}{2} - \frac{8M}{3\pi}\right)R_{onD}I_m^2 \quad (28)$$

During each switching cycle, one turn-on loss, one turn-off loss of the IGBT and one turn-off loss of the diode are

ISSN (ONLINE): 2454-9762
ISSN (PRINT): 2454-9762
Available online at www.ijarmate.com

International Journal of Advanced Research in Management, Architecture, Technology and Engineering (IJARMATE)
Vol. 3, Special Issue 10, March 2017

generated. The total average switching losses of HB-GCI within one fundamental period are calculated as

$$P_{SW\_Z} = \frac{4}{\pi} f_c E_{ts1} \frac{I_m}{I_{ac1}} \cdot \frac{U_{dc}}{U_{dc1}} \quad (29)$$

The copper loss and core loss at fundamental frequency of the filter inductor of HB-GCI is identical with the one of CMGCI. The high frequency iron loss is derived as follows. The average high-frequency magnetic flux ripple peak within one fundamental cycle is calculated as

$$\overline{\Delta B_{fe\_HBI}} = \frac{2L}{\pi N A_e f_{s1}} \int_0^{\frac{\pi}{2}} \Delta i_{HBI}\, d(t) = \frac{M}{\pi N A_e f_c} \left[U_{dc} - \frac{\pi}{4} U_{dc} E_m \right] \quad (30)$$

The high frequency iron loss of filter inductor is then calculated by substituting eqn.(30) into eqn.(22) and eqn.(23).

The RMS value of current ripple within one fundamental cycle is calculated as

$$\Delta i_{HBI\_rms} = \frac{1}{f_c} \sqrt{\frac{M^2}{6\pi L^2} \left(\frac{3}{16} \pi E_m^2 + \frac{\pi}{4} U_{dc}^2 - \frac{4}{3} U_{dc} E_m \right)} \quad (31)$$

The current THD of HB-GCI can be obtained by substituting eqn.(31) into eqn.(24).

3. Comparison of CM-GCI and HB-GCI

The actual power switch and filter inductor are selected and then the corresponding parameters in the former equations are determined according to the datasheet of the selected components. The type of the power switch is FF600R1KL4C from Infineon Technologies Co. Ltd. All of the parameters involved in the equations of the total loss and current THD are then obtained. To simulate the output character of PV array in a simple way, the reference amplitude of grid current is depicted as the following linear function of the output voltage of PV array

$$I_m^* = 0.16 U_{dc} - 8, U_{dc} \geq 200V \quad (34)$$

The distribution curves of the total losses and the current THDs corresponding to various DC output voltages of the PV array are drawn based on the former theoretical analysis results and shown in Fig. 9 and 10. When the DC voltage changes within a wide range, the total loss of the CM-GCI is always larger than the one of HB-GCI. However, the current THD and the lowest allowable DC voltage of the CM-GCI are much smaller than HB-GCI. It means that the operation range of the CM-GCI is much wider than HB-GCI.

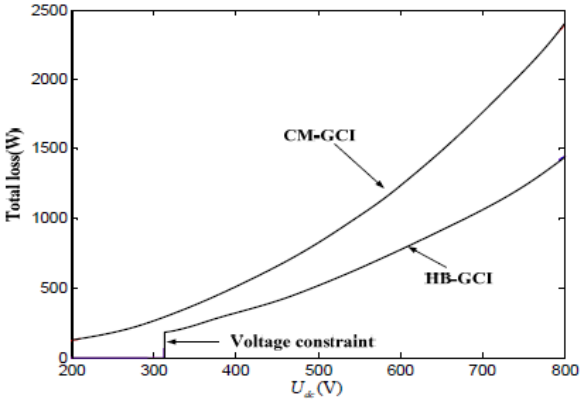

Fig. 9 Curves of total loss

The graph Fig.9 shows the variation between the total loss of Cascaded Multilevel-Grid Connected Inverter and H-Bridge Grid Connected Inverter.

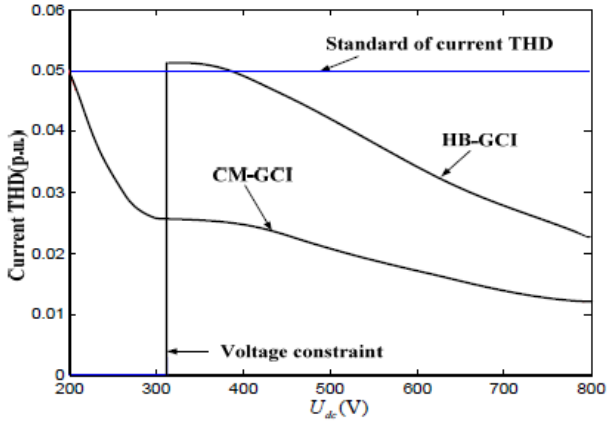

Fig. 10 Curves of current THDs

IV. RESULT AND DISCUSSION

The input voltage is first raised by the boost converter formed with inductor L1, MOSFET Q1, diode D1 and capacitor C2. If a PV array is rated for more than 50V, generally one of the input direct current busses has to be grounded per National Electric Code. The however allows some exceptions which we will discuss below. Although in theory either of two busses can be connected to earth, usually it is a negative one. It is important to remember that if DC input has a conduction pass to ground, the output AC conductors in utility-interactive configurations should be isolated from DC. In our example, a galvanicisolation is provided by a high frequency transformer in the second conversion stage. This stage is a basically a pulse-width modulated DC-DC converter. The schematic above shows a full bridge (also known as H-bridge) isolating converter comprised of Q2-Q5, T1, D2-D5, L2, and C3. For power levels under 1000 watt it could also be a half-bridge or a forward converter.

ISSN (ONLINE): 2454-9762
ISSN (PRINT): 2454-9762
Available online at www.ijarmate.com

International Journal of Advanced Research in Management, Architecture, Technology and Engineering (IJARMATE)
Vol. 3, Special Issue 10, March 2017

Single close loop control of grid current based on proportional-resonant controller (PRC) is implemented in this system. The amplitude, frequency and phase angle θ of grid voltage are estimated by the enhanced phase locked loop (EPLL).

The judgments on the two requirements are made respectively according to actual DC voltage and grid cu 55 The modulation signal *r u* output by the PR controlle solved transforming signal sw S then input the reusable CPS-SPWM to obtain the control signals of various power components.

The inverter operates in CM-GCI mode when DC voltage is lower. The output of inverter is five-level and the grid current increases gradually with the DC voltage rising. The efficiency gets a bit lower, but increases significantly when the system transforms to HB-GCI.

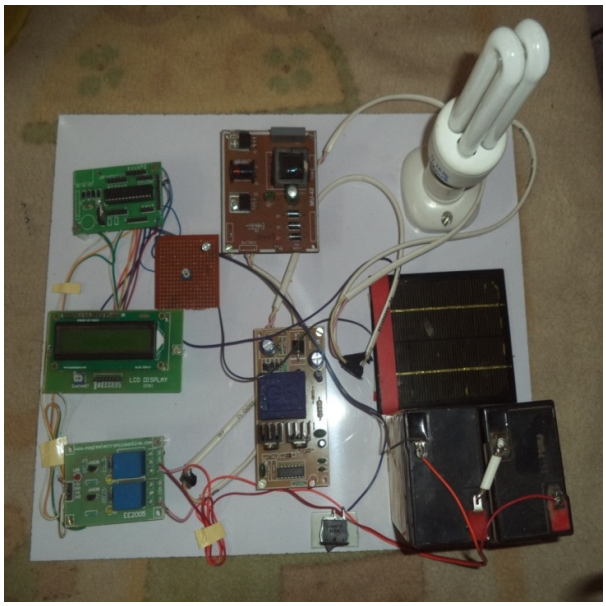

Fig. 11Hardware Model

A GTI also has to provide so-called **anti-islanding protection**. When mains fails or when its voltage level or frequency goes outside of acceptable limits, the automatic switch should SW quickly disconnect the system output from the line. The clearing time depends on the mains conditions and is specified by UL 1741. In the worse cases, when utility voltage drops below 0.5 of nominal, or its frequency deviates by +0.5 or -0.7 Hz from the rated value, GTI should cease to export power back to the grid in less than 100 milliseconds. An anti-islanding can be accomplished for example via AC under voltage or output over current detection functions. Our example depicts a system with power backup option: when contactor SW opens, the GTI will supply critical loads connected to the sub-panel.

Throughout the entire operation process, the grid current THD is limited within 5%. European efficiency of inverter is further calculated.

V. CONCLUSION

The analysis results of CM-GCI and HB-GCI indicate that, the operation range of CM-GCI is wider while the efficiency is lower. An online variable topology-type grid-connected inverter based on CM-GCI is proposed to increase the European efficiency. The detailed experimental results have proved that, with the proposed OVT-GCI, the fundamental function of controlling the grid current is implemented well and the European efficiency is increased obviously. In the proposed topology, only one extra bi-directional power switch is introduced into the cascaded multilevel invert and by proposing reusable PWM strategy, the computation of the control loop is not increased. It means that compared to standard cascaded multilevel inverter, the total cost and bulk of the proposed topology are almost not increased.

REFERENCES

[1] Ancuta F. and Cepisca C. (2011), 'Fault analysis possibilities for PV panels', Pro. International Youth Conference on Energetics, Leiria, Portugal, pp. 1 – 5.

[2] Araujo S. V. Zacharias P. and Mallwitz R. (2010), 'Highly efficient single phase transformer less inverters for grid-connected photovoltaic systems', IEEE Trans. Ind. Electron, vol. 57, no. 9, pp. 3118–3128.

[3] Berasategi A. Cabal C. and Alonso C. (2009), 'European efficiency improvement in photovoltaic applications by means of parallel connection of power converters', Pro. European Conference on Power Electronicsand Applications, Barcelona, Spain, pp. 1-10.

[4] Buticchi G. Barater D. Lorenzani E. Concari C. and Franceschini G. (2014), 'A nine-level grid-connected converter topology for single-phase transformer less PV systems', IEEE Trans. Ind. Electron, vol. 61, no. 8, pp. 3951–3960.

[5] Chen L. Amirahmadi A. Zhang Q. Kutkut N. and Batarseh I. (2014), 'Design and implementation of three-phase two-stage grid-connected module integrated converter', IEEE Trans. Power Electron, vol. 29, no.8, pp. 3881–3892.

[6] Ghartemani M. K. (2014), 'Linear and pseudo linear enhanced phased- locked loop (EPLL) structures', IEEE Trans. Ind. Electron, vol. 61, no. 3, pp. 1464–1474.

ISSN (ONLINE): 2454-9762
ISSN (PRINT): 2454-9762
Available online at www.ijarmate.com

International Journal of Advanced Research in Management, Architecture, Technology and Engineering (IJARMATE)
Vol. 3, Special Issue 10, March 2017

[7] Gmyrek Z. Boglietti A. and Cavagnino A. (2008), 'Iron loss prediction with PWM supply using low- and high-frequency measurements: analysis and results comparison', IEEE Trans. Ind. Electron, vol. 55, no. 4, pp. 1722–1728.

[8] Herran M. A. Fischer J. R. Gonzalez S. A. Judewicz M. G. and Carrica D.O. (2013), 'Adaptive dead-time compensation for grid-connected PWM inverters of single-stage PV systems', IEEE Trans. Power Electron, vol. 28, no. 6, pp. 2816–2825.

[9] Huang Y. Shen M. and Peng F. Z. (2006), 'Z-source inverter for residential photovoltaic systems', IEEE Trans. Power Electron, vol. 21, no. 6, pp. 1776–1782. [

[10] LaBella T. Yu W. Lai J. Senesky M. and Anderson D. (2014), 'A bidirectional-switch-based wide-input range high-efficiency isolated resonant converter for photovoltaic applications', IEEE Trans PowerElectron, vol. 29, no. 7, pp. 3473–3484.

[11] Liu L. Li H. Xue Y. and Liu W. (2015), 'Reactive power compensation and optimization strategy for grid-interactive cascaded photovoltaic Systems', IEEE Trans. Power Electron, vol. 30, no. 1, pp. 188–202.

[12] Nousiainen L. Puukko J. Maki A. Messo T. and Huusari J. (2013), 'Photovoltaic generator as an input source for power electronic converters', IEEE Trans. Power Electron, vol. 28, no. 6, pp. 3028–3038.

[13] Storey J. Wilson P. R. and Bagnall D. (2014), 'The optimized-string dynamic photovoltaic array', IEEE Trans. Power Electron, vol. 29, no. 4, pp. 1768–1776.

[14] Thang T. V. Thao N. M. Jang J. and Park J. (2014), 'Analysis and design of grid-connected photovoltaic systems with multiple-integrated converters and a pseudo-DC-link inverter', IEEE Trans. Ind. Electron, vol. 61, no. 9, pp. 4734–4745.

56 lalva M. G. Gazoli J. R. and Filho E. R. (2009), nprehensive approach to modeling and simulation of photovoltaic arrays', IEEE Trans. PowerElectron, vol. 24, no. 5, pp. 1198–1208.

[16] Wu J. and Chou C. (2014), 'A solar power generation system with a seven level inverter', IEEE Trans. Power Electron, vol. 29, no. 7, pp. 3454–3462.

[17] Yang Y. Zhou K. and Cheng M. (2013), 'Phase compensation resonant controller for PWM converters', IEEE Trans. Ind. Informat, vol. 9, no.2, pp. 957–964.